Percolative charge transport in binary nanocrystal solids

Luman Qu, Davis Unruh, and Gergely T. Zimanyi
Physics Department, University of California, Davis, California 95616, USA

(Received 4 January 2021; accepted 16 April 2021; published 3 May 2021)

We simulated electron transport across a binary nanocrystal solid (BNS) of PbSe NCs with diameters of 6.5 nm and 5.1 nm. We used our hierarchical nanoparticle transport simulator (HINTS) to model the transport in these BNSs. The mobility exhibits a minimum at a large-NC-fraction $f_{\mathrm{LNC}} = 0.25$. The mobility minimum is deep at $T = 80\,\mathrm{K}$ and partially smoothed at $T = 300\,\mathrm{K}$. We explain this minimum as follows. As the LNC fraction f_{LNC} starts growing from zero, the few LNCs act as traps for the electrons traversing the BNS because their relevant energy level is lower. Therefore, increasing the f_{LNC} concentration of these traps decreases the mobility. As increasing f_{LNC} reaches the percolation threshold $f_{\mathrm{LNC}}{=}f_P$, the LNCs form sample-spanning networks that enable electrons to traverse the entire BNS via these percolating LNC networks. Transport through the growing percolating LNC networks drives the rapid growth of the mobility as f_{LNC} grows past f_P. Therefore, the electron mobility exhibits a pronounced minimum as a function of f_{LNC}, centered at $f_{\mathrm{LNC}} = f_P$. The position of the mobility minimum shifts to larger LNC fractions as the electron density increases. We have studied the trends of this mobility minimum with temperature, electron density, charging energy, ligand length, and disorder. We account for the trends by a renormalized-trap model, in which capturing an electron renormalizes a deep LNC trap into a shallow trap or a kinetic obstacle, depending on the charging energy. We verified this physical picture by constructing and analyzing heat maps of the mobile electrons in the BNS.

DOI: 10.1103/PhysRevB.103.195303

I. INTRODUCTION

Colloidal semiconductor nanocrystals (NCs) are exciting nanoscale building blocks for fabricating mesoscale materials that exhibit emergent collective properties. NCs are well-defined building blocks that can be synthesized with excellent control of composition, size, and shape. The energetics and the charge transport in NC solids can be tuned by changing the NC size, size distribution, shape, inter-NC spacing, spatial ordering, surface chemistry and defects, and the properties of the matrix between the NCs. This remarkable tunability makes NC solids promising promising platforms for optoelectronic applications [1,2], including third generation solar cells [3,4], light-emitting diodes [5], and field-effect transistors (FETs) [6,7]. NC solids are especially interesting for solar cell applications because the band gap can be tuned by changing the NC size in order to improve device power conversion efficiency. Solar cell efficiency can also be improved by leveraging quantum confinement to open new energy conversion channels such as the down-converting carrier multiplication (CM), in which more than one electron-hole pairs are generated per absorbed photon [3,8–11]. CM has the potential to boost solar cell efficiency to 44%, well beyond the Shockley-Queisser limit of 33% [12]. Very recently, we have advocated for the formation of minibands in NC solar cells to implement the complementary, up-converting intermediate band solar cell paradigm [13]. In principle, intermediate-band solar cells can deliver up to 47% efficiency at one sun illumination.

One of the factors limiting the utility of NC-based optoelectronics is the relatively high energetic and spatial disorder of NC solids. This disorder causes decoherence of the electronic wave functions between NCs and inhibits the emergence of new collective mesoscale behavior, resulting instead in weakly-coupled NC films with slow hopping transport. These factors, weak coupling and slow transport are the primary agents hindering the realization of high-performance NC optoelectronics [14–16]. These factors used to limit the hopping mobility in NC solids into the range $10^{-4} - 10^{-1}\ \mathrm{cm}^2\,(\mathrm{V\,s})^{-1}$. Recently, new reasons for optimism emerged as various groups managed to boost the mobility by increasing the inter-NC charge transfer rate with a variety of methods, including ligand engineering [17–19], band alignment engineering [20], chemical doping [21,22], photodoping [23], metal-NC substitution [24], epitaxial attachment of NCs [16,25], and atomic layer deposition (ALD) infilling [26]. In some cases, these efforts managed to reach mobilities exceeding $10\ \mathrm{cm}^2\,(\mathrm{V\,s})^{-1}$ [27].

To increase the mobility even further, a deeper understanding of the role of disorder is essential. A particularly promising testing platform is the class of binary nanocrystal solids (BNSs), which are crystalline solids composed of two different types of NCs. These metamaterials can be formed from NCs of different composition and/or size [1,16,28–31]. The Murray group demonstrated the possibility of fabricating such binary nanocrystal solids as large area monolayer and bilayer structures [29]. Later, they were able to perform an *in situ* ligand exchange, producing ultrafast directional carrier transfer on the timescale of 1 ps [30]. They were also able to increase the conductivity by more than three orders of magnitude by substituting an increasing fraction of PbS NCs

with Ag or Au NCs [24]. The Alivisatos group focused on the percolation aspects of the electron transport, and beautifully imaged charge percolation pathways [28]. Whitham *et al.* devised ingenious ways to extract the localization length of the electrons in a type of percolative NC systems to further characterize transport [16].

Theoretical efforts have kept pace with these promising experimental developments only partially. A pioneering study of charge transport in NC arrays was performed by Chandler and Nelson [32]. They modeled the electronic structure of individual NCs using the $k \cdot p$ method, then performed Monte Carlo transport studies on small samples of $2 \times 2 \times 3$ and $3 \times 3 \times 4$ NCs. In the case of low charging energy, metal-insulator transitions were observed at electron occupation levels $\langle n \rangle$ that corresponded to the complete filling of an s, p, or d shell. When the charging energy became comparable to the level broadening, additional minima appeared in the conductance at every integer value of $\langle n \rangle$ as a result of electron-electron repulsion. The charge transport properties of NCs embedded in a matrix were explored by others using a kinetic Monte Carlo (KMC) method [33,34]. Although these papers developed an advanced method that was capable of handling the long-range Coulomb interactions, the small system sizes limited the definitiveness of their conclusions.

Our first contribution to this field was to develop the kinetic Monte Carlo platform HINTS—the hierarchical nanoparticle transport simulator—to compute the electron and hole mobilities as a function of the NC diameter [35]. We found that the mobility exhibited a maximum or plateau as a function of the NC diameter (depending on the type of disorder). This finding was in agreement with corresponding experiments [36,37]. Since then, we extended HINTS to describe the metal-insulator transition in NC solids and proposed a quantum percolation model to explain the unique criticality observed [[38], see also [39]]. Very recently, we demonstrated that NC solids are an excellent platform to study Mott-Hubbard phenomena, as they exhibit transport transitions driven by interactions, by disorder, and by their interplay [40].

In this paper, we adapt and apply our hierarchical transport simulator HINTS [35,38] to study charge transport in BNSs consisting of PbSe NCs of two different sizes. Our simulation results are motivated by early stage efforts to measure the transport of such binary NC films fabricated with layer-by-layer dip coating of colloidal mixtures. Our main results include the following. First, our HINTS simulations of the mobility of field-effect transistors made from PbSe NCs with a mixture of 6.5 nm diameter large NCs (LNCs), and 5.1 nm diameter small NCs (SNCs) showed a deep minimum at a fraction of the LNCs, $f_{\mathrm{LNC}} = 0.25$. The minimum persists up to temperatures where kT becomes comparable to the difference of the conduction-band edge energies of the LNCs and SNCs. We developed a percolative theory to explain this deep mobility minimum. We propose that at low f_{LNC}, the LNCs form traps and thus suppress the mobility. With increasing f_{LNC}, these LNC traps coalesce into a percolative transport pathway at $f_{\mathrm{LNC}} = f_{\mathrm{P}}$. f_{LNC} increasing beyond f_{P} opens a new transport channel: the electrons propagating through the percolating LNCs. This new channel starts boosting transport with increasing f_{LNC}, thereby explaining the mobility minimum. Second, we analyzed the impact of NC site energy disorder, carrier density, charging energy, and ligand length on the transport. We developed an electron-occupation-induced trap renormalization model that accounted for the dependence of the mobility on these four parameters. Finally, we validated our percolative theory of LNC traps transforming into percolative transport pathways as a function of f_{LNC} by constructing and analyzing heat maps of the carrier residence times.

II. OVERVIEW OF SIMULATION AND RESULTS

For this paper, we extended and adapted our previously developed HINTS to describe transport in binary NC solids. The presentation and discussion of our results requires a brief description of the hierarchical levels of HINTS (described in more detail in the Supplemental Material [41]).

(1) We used the event-driven molecular dynamics code PackLSD [42] to generate a random-packed, jammed NC solid for the simulation. The NC solids typically included many hundred NCs with a form factor of $10 \times 10 \times 1$, inspired by the experimental geometry of 2D FET channels. For example, a monodisperse sample containing 400 NCs was packed into a simulation volume with the approximate spatial extent of $16 \times 16 \times 1.6$ NC diameters. It is noted here that due to the form factor of these NC solids, short-range processes can have 3D character, phenomena driven by long range correlations, such as phase transitions, are effectively 2D. For the binary NC solids, the diameters of the SNCs and LNCs were selected from corresponding Gaussian distributions, with widths σ_{SNC} and σ_{LNC}, and then jam-packed to form the binary NC solid BNS. We note that experimentally the amount of disorder in the NC solid can be tuned, from an approximately ordered solid to a more disordered solid, with some degree of glassiness.

(2) Next, the energy parameters of the Hamiltonian of each NC were established as follows. We used the photoelectron spectroscopy results of Jasieniak *et al.* [43] modified by the method of Miller *et al.* [44] to estimate the energies of the valence band maximum (E_{VBM}) and conduction band minimum (E_{CBM}) of PbSe NCs as a function of NC diameter. These energies are modified, or tuned, from their bulk values by quantum confinement, the fact that the electron wave functions are localized on the NCs. The values are plotted in Fig. 1. Photoelectron spectroscopy provides a direct measurement of E_{VBM}, from which E_{CBM} can be estimated by adding the NC band gap. Following Jasieniak *et al.*, we show limiting values of E_{CBM} obtained using the experimentally-determined optical band gap ($E_{\mathrm{CBM,optical}}$) and a calculated upper estimate of the electronic band gap, which includes Coulomb and polarization energies ($E_{\mathrm{CBM,max}}$), yielding a range of E_{CBM} values for each NC size (green band in Fig. 1). Clearly, E_{CBM} exhibits a much larger change with NC size than does E_{VBM}. For example, 75–85% of the difference in band gap for 5.1 nm and 6.5 nm NCs is due to the change in E_{CBM}, with the exact value depending on the true electronic band gap of the PbSe NC. Building on these experimental findings, for our HINTS simulations we used the E_{CBM} curve from the $k \cdot p$ calculations of Kang and Wise (dashed line in Fig. 1) [45], which is well-validated by its dependence on the NC size closely tracking the experimental $E_{\mathrm{CBM,max}}$ values.

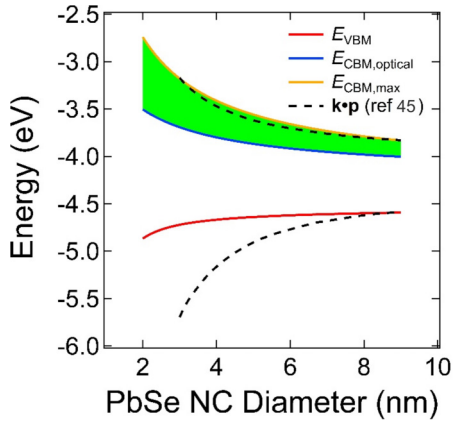

FIG. 1. Absolute conduction and valence band edge energies (E_{CBM} and E_{VBM}) of PbSe NCs as a function of NC diameter. E_{VBM} was measured by photoelectron spectroscopy [43,44]. E_{CBM} has a range of values (green band) bracketed by E_{CBM}, optical (from the measured optical band gap) and $E_{CBM,max}$ (from a DFT-calculated upper estimate of the electronic band gap). Also shown are the E_{CBM} and E_{VBM} curves calculated from $k \cdot p$ theory (dashed lines, Ref. [45]), rigidly shifted along the ordinate to match the experimental data at large NC size. The latter E_{CBM} curve is used to parametrize our transport model. Contribution to this figure by Matt Law is gratefully acknowledged.

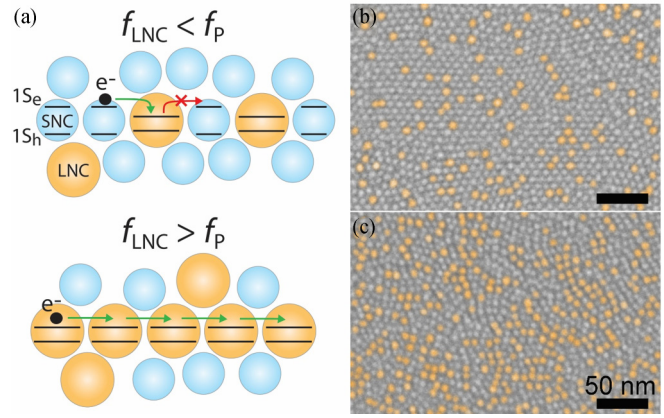

FIG. 2. (a) Schematic representation of a binary NC solid containing (top) a small fraction of LNCs and (bottom) a larger fraction of LNCs. When $f_{LNC} < f_P$, the LNCs act as isolated carrier traps, impeding transport. When $f_{LNC} > f_P$, the LNCs form contiguous low-energy transport pathways that facilitate transport. (b), (c) Colorized SEM images of a monolayer of a binary NC solid made from 6.5 nm and 5.1 nm PbSe NCs with (b) $f_{LNC} = 0.12$ ($< f_P$) and (c) $f_{LNC} = 0.31$ ($> f_P$). The LNCs are shaded orange. LNC percolation pathways are evident in the latter image. The NCs are capped by oleate ligands (prior to exchange with EDT). Scale bars are 50 nm. SEM image is courtesy of Matt Law, UC Irvine.

Our model also includes the electron-electron interaction at the level of an on-site self-charging energy E_C. This charging energy can be calculated by a variety of methods, including the semiempirical pseudopotential configuration interaction (CI) method of Zunger and coworkers [46,47], and the tight-binding many body perturbation theory method of Delerue [48,49]. In this paper, we report results with the latter approach, selected for its versatility. The long-range part of the Coulomb interaction plays a noticeable part only at low temperatures, and thus can be disregarded for many applications such as solar cells.

(3) We modelled the transport of charge carriers between adjacent NCs as Miller-Abrahams phonon-assisted tunneling, also called thermally activated hopping. An alternate model is the Marcus theory of multiphonon activated transitions. We have coded up Marcus hopping as well, but did not use it here as the Miller-Abrahams model is a more accurate description at higher temperatures. Importantly, the physical explanations we develop below for the observed phenomena are insensitive and independent from the details of the NC-NC hopping, and thus there is every reason to believe that repeating the simulations with Marcus hopping would produce qualitatively the same results. The inter-NC distance was set at twice the ligand length. The tunneling probabilities between NCs were determined by the standard WKB form.

(4) We simulated the transport across the BNS using the extended kinetic Monte Carlo method with activated hopping transitions between nearest-neighbor NCs [35,50]. Electrons were added to the BNS at random with a specified average electron density (e/NC). Then the electrons were allowed to relax to favorable energy configurations. Transport was simulated by applying an electric field and measuring the responsive current. The simulation was run for a sufficiently long time to ensure that the carrier flow reached a steady state. The electric fields were kept sufficiently small to ensure that the transport was in the linear response regime. The carrier mobility was extracted from the slope of the linear I-V curves. The overall NC-NC hopping attempt rate prefactor was selected such that the simulated mobilities were consistent with published experimental values [36]. We systematically explored wide ranges of temperature, disorder, electron density, and Coulomb interaction. The mobilities were determined by simulating at least 40 samples, and often more than 100 samples, at each set of parameters and then averaging the results. Since each mobility was determined from a dynamic flow of hundreds of electrons over 105–106-time steps, we achieved a remarkably good self-averaging with small error bars even with this moderate number of samples.

Next, we describe the experimental motivation for our work, the main simulation results obtained using HINTS, and the physical picture emerging from the simulations.

Figure 2(a) illustrates charge transport in a binary PbSe NC solid. Quantum confinement modifies the $1S_e$-$1S_h$ band gaps of the LNCs to be smaller than those of the SNCs, and the $1S_e$ energies (i.e., E_{CBM}) of the LNCs lower than those of the SNCs. Therefore, in a binary NC solid with a small f_{LNC} fraction, the LNCs act as traps for the mobile electrons [Fig. 2(a), top]. Accordingly, as f_{LNC} is increased from small values, the increasing trap density causes a monotonic decrease of the carrier mobility.

Increasing f_{LNC} first enables the LNCs to form clusters, and then increases the size of the LNC clusters in the BNS. Once f_{LNC} exceeds the percolation threshold f_P, the LNC clusters interconnect to form contiguous percolation networks that span the entire BNS. These LNC percolation networks open new transport channels: low-energy, low-disorder and

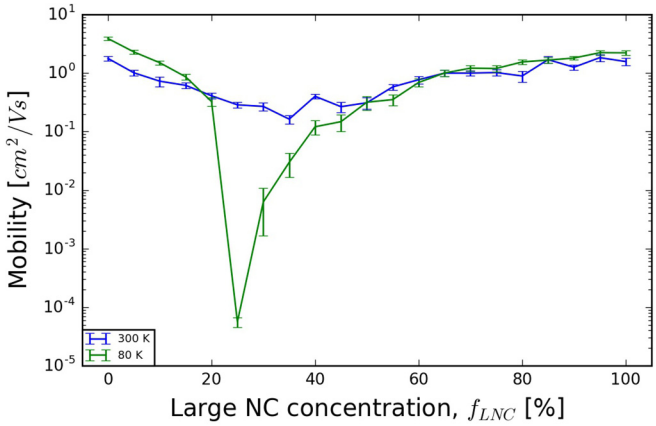

FIG. 3. Simulated electron mobility versus f_{LNC} for 6.5 nm and 5.1 nm PbSe NCs. $\Delta E_{\mathrm{CBM}} = 60$ meV; with a diameter disorder of $\sigma_{\mathrm{LNC}} = 0.325$ nm and $\sigma_{\mathrm{SNC}} = 0.046$ nm; and electron density $n = 0.25\ e$/NC.

thus high-mobility transport pathways [Fig. 2(a), bottom]. As $f_{\mathrm{LNC}} \rightarrow 1$, the percolation networks densify and the mobility steadily increases toward its value in a monodisperse NC solid, formed only from LNCs.

Figures 2(b) and 2(c) compare scanning electron microscopic images of monolayer-thick films of oleate-capped 6.5 nm and 5.1 nm PbSe NCs having f_{LNC} fractions below and above f_{P}. For $f_{\mathrm{LNC}} = 0.31$ ($> f_{\mathrm{P}}$), the LNCs (colored orange) visibly form essentially sample-spanning clusters. These images show that the LNCs are well mixed in the SNC films and have no tendency to phase separate into pure LNC domains.

Before proceeding, a word about the experimental systems. The binary NC films were made by layer-by-layer dip coating of colloidal mixtures of 6.5 nm and 5.1 nm PbSe NCs. The NCs were synthesized by the hot injection method. Colloidal solutions of different LNC number fraction (f_{LNC}) were prepared in hexane, dip coated onto prepatterned field-effect transistor (FET) substrates using ligand exchange with 1,2-ethanedithiol (EDT), and then infilled and overcoated with amorphous alumina using low-temperature atomic layer deposition (ALD), yielding transistors with dominant n-channel (electron) transport, excellent stability, and greatly-reduced *I-V* hysteresis compared to EDT-treated NC FETs before ALD infilling [51]. The f_{LNC} values of the resulting films were confirmed by analyzing SEM images of the first NC monolayer in the FET channel [like those in Figs. 2(b) and 2(c)]. The experimental methods are described in further details in the Supplemental Material [41]. We continue with presenting the results of our simulations.

A. Mobility as a function of LNC fraction f_{LNC}

Figure 3 presents the HINTS-simulated mobility of a PbSe BNS with NC diameters of 6.5 nm and 5.1 nm at $T = 80$ K and 300 K. The corresponding difference of the SNC and LNC conduction band energy minima was taken from Fig. 1 as $\Delta E_{\mathrm{CBM}} = 60$ meV; for other parameters see the Supplemental Material [41]. The simulated mobility curve at $T = 80$ K shows a deep mobility minimum at $f_{\mathrm{LNC}} = 0.25$. Interpreting f_{LNC} of this minimum as approximately equal to f_{P}, the geometric percolation fraction is consistent with the prediction of $f_{\mathrm{P}} = 0.24$ of bond percolation theory [52], as well as with the percolation onset of $f_{\mathrm{P}} = 0.22$, observed in our recent calculations of NC films [38]. The precise relationship between the position of the mobility minimum and f_{P} is impacted by the NC packing and the electron density, as discussed below.

Another feature is that the mobility of the monodisperse solid of LNCs ($f_{\mathrm{LNC}} = 1.0$) is smaller than, or equal to, the mobility of the monodisperse solid of SNCs ($f_{\mathrm{LNC}} = 0$). This feature seems to contrast the previous reports [14,35] that electron mobility increases with NC size. However, in our simulations, the LNCs have a larger size disorder than the SNCs, large enough to offset the expected gain in mobility from an increasing NC diameter.

The key message of this simulation is the emergence of a mobility minimum as a function of f_{LNC} around f_{LNC}=f_{P}, which is sharp and deep at low temperatures, and partially smoothed at higher temperatures. As mentioned earlier, we developed a percolative theory to explain this deep mobility minimum. We propose that as the lower-energy LNCs are introduced into the higher-energy SNC matrix at low f_{LNC}, the LNCs form traps and thus suppress the electron mobility. With increasing f_{LNC}, these LNC traps coalesce into a percolative transport pathway at $f_{\mathrm{LNC}} = f_{\mathrm{P}}$. Once f_{LNC} increases beyond f_{P}, the electrons can propagate through this percolating network of LNCs, thus opening up a new transport pathway. As f_{LNC} grows past $f_{\mathrm{P}} \rightarrow 1$, the percolating networks densify and the mobility steadily increases toward its value in a monodisperse NC solid, formed only from LNCs. The opening of this new percolating LNC transport channel at $f_{\mathrm{LNC}} = f_{\mathrm{P}}$, and its subsequent broadening as f_{LNC} grows past f_{P} explains the mobility minimum.

B. Mobility as a function of temperature *T*

The mobility minimum is considerably smoothed out as the temperature is raised from T=80 K to T=300 K. The mobility at the minimum rises by a bit more than three orders of magnitude. The ratio of the mobilities at the minimum for the two temperatures is consistent with an estimate based on an activated transport across a gap of $\Delta E_{\mathrm{CBM}} = 60$ meV. Of course, the precise value of the mobility is further impacted by f_{LNC}, and the electron density as well.

We add that more complex behaviors can emerge as a function of temperature. The depth of the mobility minimum is controlled by the f_{LNC} fraction of the LNCs in the BNS and the thermal activation factor $\exp(-\Delta/\mathrm{k}_B T)$, corresponding to an electron hopping from an LNC trap to an SNC. In a first approximation, the Δ energy barrier faced by an electron in an LNC trap can be identified with ΔE_{CBM}. However, for traps that are already occupied, the trap energy Δ is renormalized to the smaller value of $\Delta_r = \Delta E_{\mathrm{CBM}} - \mathrm{E}_C$, as long as $\Delta E_{\mathrm{CBM}} > \mathrm{E}_{\mathrm{C}}$. Next, it is recalled that Kang *et al.* reported that some experiments can be explained by assuming that the charging energy E_{C} depends on the temperature to a substantial degree: $\mathrm{E}_{\mathrm{C}} = \mathrm{E}_{\mathrm{C}}(T)$ [53]. In their work, Kang *et al.* reported a 40–70% increase of $\mathrm{E}_{\mathrm{C}}(T)$ as the temperature was raised from $T = 20$ K to 80 K. A charging energy $\mathrm{E}_{\mathrm{C}}(T)$ that increases with temperature creates a renormalized

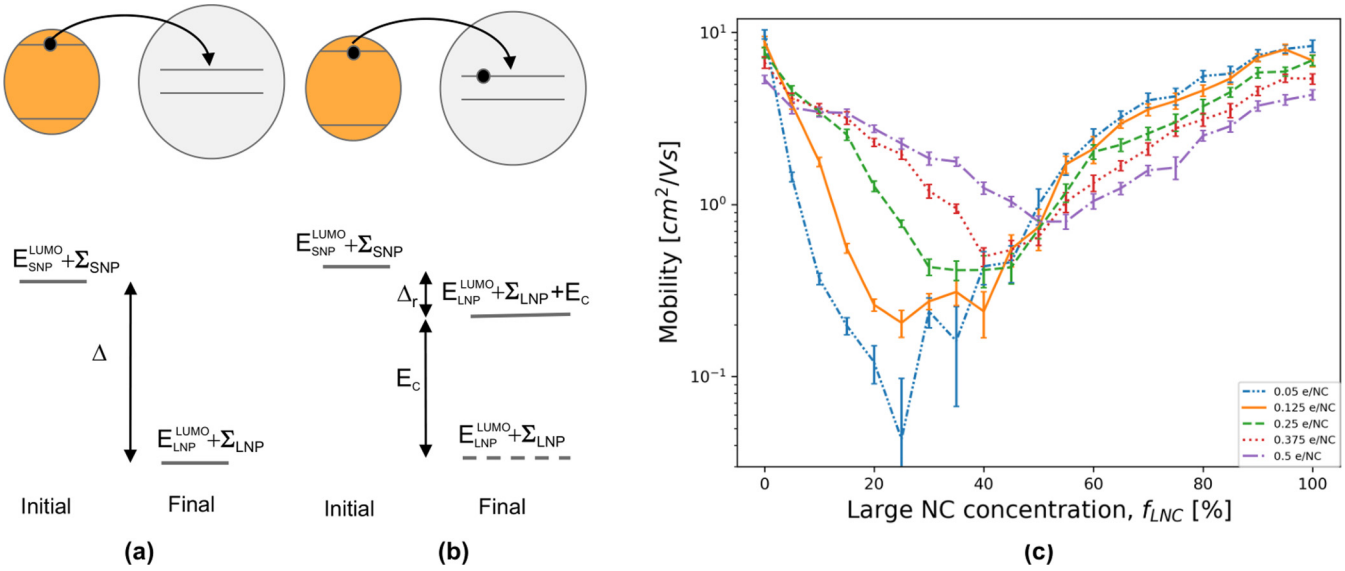

FIG. 4. Impact of electron density when $E_C < \Delta$. (a) Energy levels of the initial state and the final state of an electron hopping from an SNC on an unoccupied trap of an LNC. (b) Energy levels of the initial state and the final state of an electron hopping from an SNC on a singly occupied trap of an LNC. The unchanging energy of the electron already on the LNC is not shown expressly for clarity. The dashed level shows the energy without the charging energy E_C for reference. (c) Mobility vs. f_{LNC} for electron densities from 0.05 e/NC to 0.5 e/NC at $T = 80$ K, with $\sigma_{SNC} = 0.01$ nm and $\sigma_{LNC} = 0.08$ nm for $E_C < \Delta$. The mobility at zero LNC concentration is higher than in Fig. 3, because the disorder of the SNC diameters, σ_{SNC}, is four times smaller than in Fig. 3.

trap energy $\Delta_r(T)$ that decreases with increasing temperature. This mechanism can explain a smoothing of the mobility minimum with the temperature that is faster than a smoothing driven by temperature-independent energy parameters alone.

Remarkably, the opposite scenario can arise as well. If $\Delta E_{CBM} \gg E_C$, then several electrons can occupy each trap. This creates effective traps whose energy spectrum is a ladder with E_C level spacing, and thus E_C plays the role of the renormalized trap energy $\Delta_r = E_C(T)$. In this parameter range, a Kang-type temperature-dependent charging energy creates a renormalized gap $\Delta_r(T)$ that increases with increasing temperature, making the high-temperature mobility minimum deeper than the one corresponding to temperature-independent parameters.

The above considerations motivate us to investigate the behavior of the BNS mobility in different parameter ranges, and to use our interaction-renormalized trap model to analyze and interpret our results. This is what we do in the rest of this paper.

C. Mobility as a function of electron density *n* and charging energy E_C

The electrostatic effects of adding electrons to a NC are taken into account following the work of Delerue [48,49]. When an electron is added to a neutral NC at the bottom of the conduction band, the E_{CBM} energy is increased by the one-electron self-energy, Σ, arising from the charging of the NC, also including the effect of the NC's polarizable host. When a second electron is added, the screened repulsion between the two electrons costs an additional charging energy E_C (denoted as U by Delerue). When the KMC step of HINTS evaluates the probability of a jump from one NC to another NC, the difference between the total initial energy and total final energy is calculated, including these electrostatic energies. The details of the HINTS code are described in the Supplemental Material [41].

When a LNC is unoccupied within a SNC matrix, it is a trap with a depth for an electron. Δ is given by the difference of the CBM energies of the LNC and the SNC, ΔE_{CBM}, plus the difference of the self-energies $\Sigma_{LNC} - \Sigma_{SNC}$: $\Delta = \Delta E_{CBM} + (\Sigma_{LNC} - \Sigma_{SNC})$. When the trap is already occupied by an electron, the trap energy Δ gets renormalized by the charging energy E_C to $\Delta_r = \Delta - E_C$. For $E_C < \Delta$, this renormalization transforms the deep traps into shallow traps, making them much less efficient in hindering transport. For $E_C > \Delta$, this renormalization transforms the LNCs from negative-energy traps into positive-energy obstacles.

We explore the effects of varying the charging energy by simulations using $E_{C,LNC} = E_{C,SNC} = E_C = 35$, and $E_{C,LNC} = E_{C,SNC} = E_C = 125$ meV, in order to explore both relevant regimes of $E_C < \Delta$, and $E_C > \Delta$. The effects of the charging energy E_C are closely interdependent with that of the electron density n. We therefore explored the average electron density n sweeping across $n = 0 - 0.5$ e/NC, because most density-dependent phenomena are cyclic with a n period of 1. Therefore, in the complementary range of $n = 0.5 - 1.0$ e/NC, the mobility's behavior is the approximate mirror image across $n = 0.5$, and for $n > 1$, the entire cycle repeats.

Figures 4 and 5 show simulation results for small and large E_C. In both cases, the mobility minimum gets shifted to larger f_{LNC} concentrations as the electron density n grows. The primary reason for this is trap renormalization by electron occupancy. As the electrons are introduced into the sample, they fill up the LNC traps, renormalizing them into shallower traps, or possibly into obstacles. For $n < f_{LNC}$, this reduces the number of deep, unrenormalized traps, which are the primarily suppressants of the mobility. As the

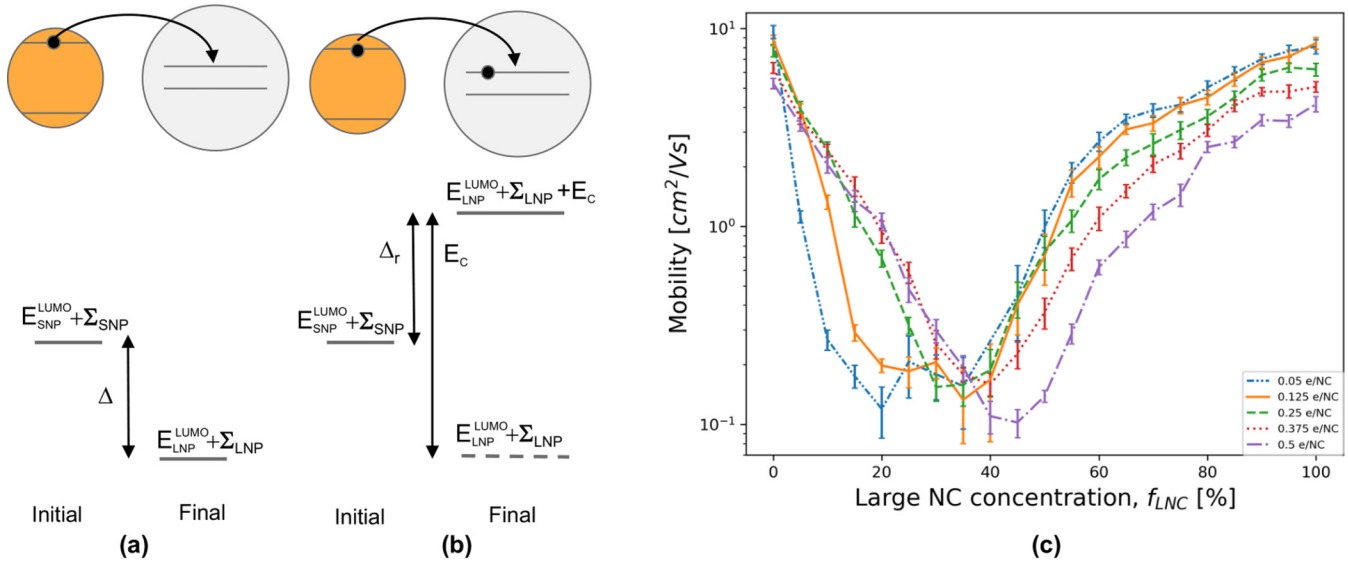

FIG. 5. Impact of electron density when $\mathbf{E_C} > \Delta$. (a) Energy levels of the initial state and the final state of an electron hopping from an SNC on an unoccupied trap of an LNC. (b) Energy levels of the initial state and the final state of an electron hopping from an SNC on a singly occupied trap of an LNC. The starting energy of the electron already on the LNC is not shown expressly for clarity. The dashed level shows the energy without the charging energy E_C for reference. (c) Mobility vs f_{LNC} for electron densities from 0.05 e/NC to 0.5 e/NC at $T = 80$ K, with $\sigma_{SNC} = 0.01$ nm and $\sigma_{LNC} = 0.08$ nm for $E_C > \Delta$.

electron density exceeds the LNC density, $n > f_{LNC}$, a trapped electron population equal to the number of LNCs dynamically renormalizes essentially all deep trap LNCs into shallow traps. This leaves the nontrapped excess $(n - f_{LNC})$ electrons to move across the BNS that has the same trap density, but which are now renormalized into shallow traps. In reverse, the $(n - f_{LNC})$ density of nontrapped electrons decreases as f_{LNC} increases, thereby decreasing the mobility. Once f_{LNC} exceeds n, the mobility keeps decreasing with f_{LNC} until the unrenormalized deep traps percolate. The percolation of the unfilled/unrenormalized deep traps is only reached at f_{LNC} concentrations that exceed f_P by a quantity set by n. This explains the mobility minimum moving to higher f_{LNC} concentrations with increasing n.

Figure 4 shows that when E_C is small (35 meV), and thus $E_C < \Delta$, increasing n shifts the mobility minimum to higher f_{LNC}, as well as makes the minima shallower. Figure 5 shows that when E_C is large, $E_C > \Delta$, increasing n again shifts the mobility minimum to higher f_{LNC}, but without changing its depth. In the case of Fig. 4, LNCs with one trapped electron remain energetically capable of trapping additional electrons, as renormalized shallow traps Δ_r. In this situation, increasing n fills an increasing fraction of the LNCs with electrons, thereby decreasing the average trap energy in the NC film and thus resulting in a shallower and shallower mobility minimum. In addition, shallow traps next to deep traps make it easier for the trapped electrons to escape from the deep traps via a two-step process, thus further reducing the depth of the mobility minimum.

Figure 5 shows that for large E_C (125 meV), since $E_C > \Delta$, the LNCs that have trapped one electron become energetically incapable of trapping an additional electron, and are thus transformed into kinetic obstacles against transport. Therefore, each singly-occupied LNC becomes a lost trap, so increasing n again shifts the mobility minimum to higher f_{LNC}, but the average trap energy remains unchanged, and thus the depth of the minimum remains unchanged too, as shown in Fig. 5. In addition, increasing n increases the mobility at low f_{LNC} values.

D. Mobility as a function of size disorder

We briefly explored the effect of LNC size polydispersity on transport. Figure 6 compares mobilities for LNC polydispersities of $\Sigma_{LNC} = 0.08$ nm and 0.16 nm. We find that such an increase in polydispersity decreases the depth of the mobility minimum without changing its position. The site energy disorder, induced by the LNC polydispersity, has competing effects. Increasing disorder tends to decrease the mobility on the LNC network itself. However, this same increased variation of the site energies makes some of the LNCs into

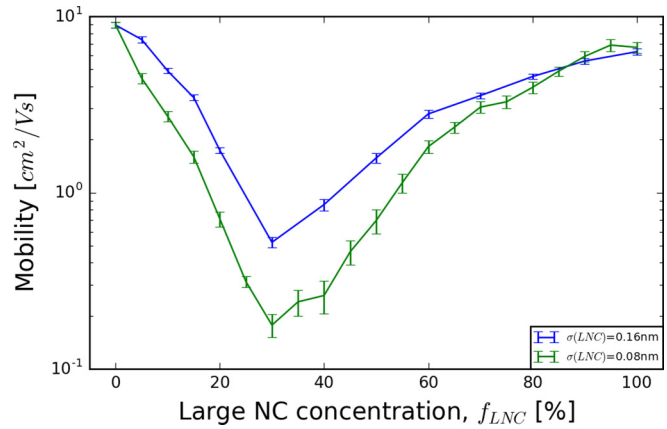

FIG. 6. Mobility vs f_{LNC} for an LNC size polydispersity of $\sigma_{LNC} = 0.08$ nm and $\sigma_{LNC} = 0.16$ nm. Electron density = 0.25 e/NC; $T = 80$ K; SNC polydispersity $\sigma_{SNC} = 0.01$ nm; $E_C = 35$ meV.

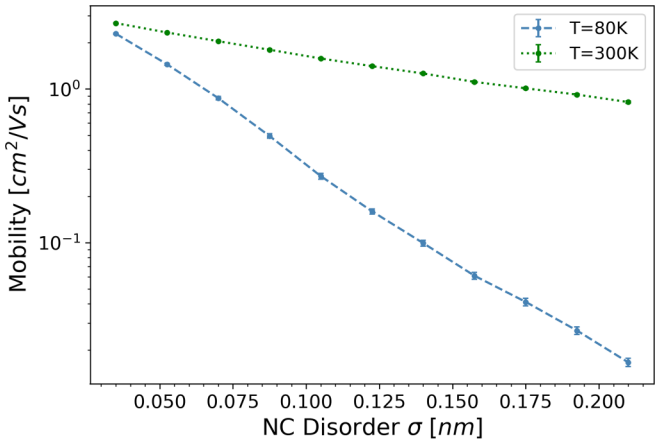

FIG. 7. Mobility vs NC size polydispersity σ, at $T = 80$ K and $T = 300$ K. Monodisperse NC solids with mean diameter = 3.5 nm; electron density = 0.25 e/NC.

shallower traps, enhancing the mobility. In the present case, the latter of the two effects seems to be more impactful.

For completeness, we also explored the effect of size polydispersity, or simply size disorder, on transport in a NC solid with NC diameters distributed according to a single Gaussian centered on a mean of 3.5 nm. Figure 7 shows the mobility as the size disorder is increased at two different temperatures, $T = 80$ K and $T = 300$ K. Without the competing effects described above in the context of BNSs, in polydisperse NC solids with a Gaussian size distribution increasing disorder simply supresses the mobility, and drives the NC solid further into a disorder-localized phase.

E. Mobility as a function of ligand length

We simulated transport for ligand lengths of 0.6 nm and 0.8 nm, resulting in NC-NC separations of 1.2 nm and 1.6 nm, respectively. The larger inter-NC spacing reduces the entire mobility curve by a multiplicative factor, the ratio of the tunneling factors that depend on the ligand length exponentially. Varying the ligand length did not change the depth or position of the mobility minimum.

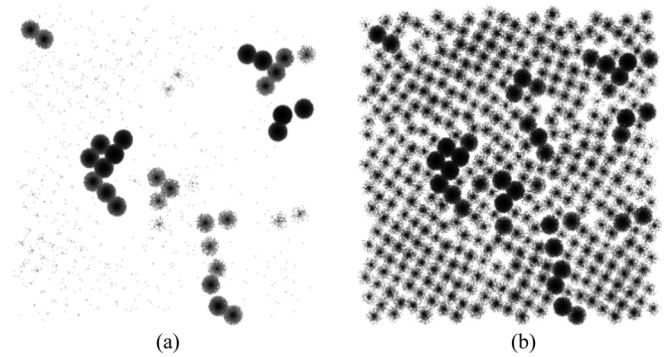

FIG. 9. Temperature dependence of the electron occupancy maps for a typical BNS at (a) $T = 80$ K and (b) $T = 300$ K.

F. Transport heat maps

We visualized the transport through the percolating network by building heat maps that show the time-integrated electron occupancy for each NC during the simulation. At periodic instants we recorded the location of each electron, and overlaid all these images. Thus, an NC appearing darker indicates more electrons spending longer times on that NC. Figures 8 and 9 show heat maps for several different f_{LNC} values, with an electron density equal to 0.25 e/NC in a BNS with $\mathrm{E_C} < \Delta$. At $f_{\mathrm{LNC}} = 0$, the sample consists only of SNCs: the heat map is very homogeneous, and the mobility is high. At $f_{\mathrm{LNC}} = 0.05$, the LNCs act as isolated traps, but most electrons can avoid the sparse traps and propagate via the SNC matrix. For $f_{\mathrm{LNC}} = 0.10$, the LNC traps start to capture

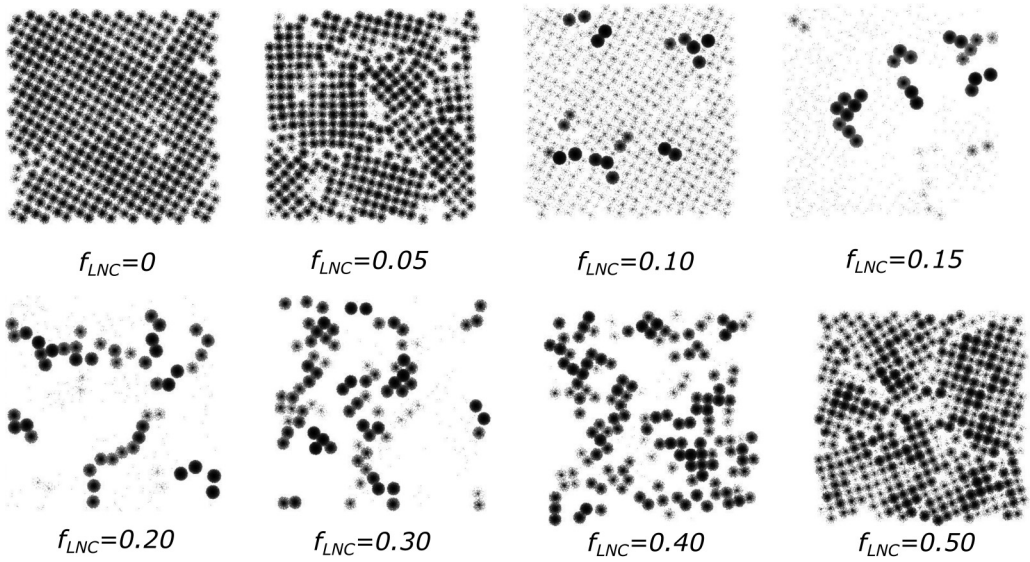

FIG. 8. Electron occupancy heat maps for a typical BNS for different values of f_{LNC}. Shading indicates the time-integrated probability of each NC being occupied by electrons.

a substantial fraction of the propagating electrons. For $f_{LNC} = 0.15$, most the electrons spend most of their time captured in the LNC traps. These traps are isolated, or form small clusters. At $f_{LNC} = 0.20$, the LNC clusters nearly interconnect. The mobility decreases in the entire range of LNC concentrations from $f_{LNC} = 0$ to $f_{LNC} = 0.20$.

At $f_{LNC} = 0.30$, the first sample-spanning LNC clusters appeared. The formation of these percolation networks causes the mobility to begin increasing. At $f_{LNC} = 0.40$, the percolation networks densify, greatly helping the mobility to recover. Finally, at $f_{LNC} = 1.00$, the occupancy heat map becomes quite homogeneous, comparable to the map at $f_{LNC} = 0$. These images give a clear visual support to the physical picture developed above: as f_{LNC} starts to increase from zero, the LNCs serve as traps and thus suppress the mobility. When the LNCs percolate, then the traps suddenly form new transport channels and start increasing the mobility. Therefore, the mobility forms a minimum at the percolation threshold f_P, modified by the electron density n. As f_{LNC} grows towards $f_{LNC} = 1.00$, the transport can again flow through the entire NC matrix.

Figure 9 shows the effect of temperature on the heat maps of a typical BNS. Electron transport pathways are dominated by the deep traps at $T = 80$ K, giving rise to a very uneven heat map. At $T = 300$ K, thermal energy is reasonably effective at freeing the trapped electrons, so the electron transport is more homogeneous throughout the sample. This translates to a higher mobility at higher temperatures, which is consistent with the smoothing out of the mobility minimum at $T = 300$ K, reported above in Fig. 3.

III. DISCUSSION AND CONCLUSIONS

We simulated and fabricated field-effect transistors (FETs) made from a mixture of PbSe NCs with diameters of 6.5 nm and 5.1 nm, thereby forming a binary nanocrystal solid (BNS). We used our hierarchical nanoparticle transport simulator to model the transport in these BNSs, and study the impact of several factors on this transport. The BNS mobility exhibited a minimum at a large-NC-fraction $f_{LNC} = 0.25$. The mobility minimum was deep at $T = 80$ K and partially smoothed at $T = 300$ K. We developed the following physical picture to account for this behavior. As the LNC fraction f_{LNC} within the SNC matrix starts growing from zero, the few LNCs act as deep traps for the electrons traversing the SNC matrix. Increasing the f_{LNC} concentration of these traps decreases the mobility. As the increasing f_{LNC} reaches the percolation threshold $f_{LNC} = f_P$, the LNCs form sample-spanning networks that enable electrons to traverse the entire BNS via low-energy, low-disorder LNC pathways. The opening of the new transport channel through these percolating LNC pathways leads to the recovery of the mobility as f_{LNC} grows past f_P. Therefore, the electron mobility exhibits a pronounced minimum as a function of f_{LNC} at $f_{LNC} = f_P$. We have studied the effect of temperature, electron density, charging energy, ligand length, and disorder on the mobility minimum. To account for all trends, we have proposed that capturing an electron renormalizes a deep trap LNCs into either a shallow trap or a kinetic obstacle, depending on the value of the charging energy E_C relative to the NC energy difference Δ. A central prediction of this model is that the position of the mobility minimum shifts to a larger LNC fraction $f_{LNC} > f_P$ as the electron density increases, but its depth is modified differently depending on whether $E_C < \Delta$, or $E_C > \Delta$. Finally, we verified our expectations and physical picture by constructing and analyzing heat maps of the mobile electrons in the simulated BNS.

ACKNOWLEDGMENTS

The authors thank Nicholas Brawand, Ian Carbone, Giulia Galli, Victor Klimov, Art Nozik, Boris Shklovskii, Márton Vörös, and especially Matt Law for many useful discussions. This work was supported by the National Science Foundation under award DMR-2005210.

[1] D. V. Talapin, J.-S. Lee, M. V. Kovalenko, and E. V. Shevchenko, Chem. Rev. **110**, 389 (2010).
[2] M. V. Kovalenko, L. Manna, A. Cabot, Z. Hens, D. V. Talapin, C. R. Kagan, V. I. Klimov, A. L. Rogach, P. Reiss, and D. J. Milliron *et al.*, ACS Nano **9**, 1012 (2015).
[3] A. J. Nozik, Physica E: Low-dimensional Systems and Nanostructures **14**, 115 (2002).
[4] P. V. Kamat, J. Phys. Chem. C **112**, 18737 (2008).
[5] Y. Shirasaki, G. J. Supran, M. G. Bawendi, and V. Bulović, Nat. Photonics **7**, 13 (2013).
[6] D. V. Talapinand C. B. Murray, Science **310**, 86 (2005).
[7] F. Hetsch, N. Zhao, S. V. Kershaw, and A. L. Rogach, Mater. Today **16**, 312 (2013).
[8] S. Wippermann, M. Vörös, D. Rocca, A. Gali, G. Zimanyi, and G. Galli, Phys. Rev. Lett. **110**, 046804 (2013).
[9] M. Vörös, D. Rocca, G. Galli, G. T. Zimanyi, and A. Gali, Phys. Rev. B **87**, 155402 (2013).
[10] M. Vörös, S. Wippermann, B. Somogyi, A. Gali, D. Rocca, G. Galli, and G. T. Zimanyi, J. Mater. Chem. A **2**, 9820 (2014).
[11] M. Govoni, I. Marri, and S. Ossicini, Nat. Photonics **6**, 672 (2012).
[12] W. Shockley and H. J. Queisser, J. Appl. Phys. **32**, 510 (1961).
[13] M. Vörös, G. Galli, and G. T. Zimanyi, ACS Nano **9**, 6882 (2015).
[14] Y. Liu, M. Gibbs, J. Puthussery, S. Gaik, R. Ihly, H. W. Hillhouse, and M. Law, Nano Lett. **10**, 1960 (2010).
[15] E. Kalesaki, W. H. Evers, G. Allan, D. Vanmaekelbergh, and C. Delerue, Phys. Rev. B **88**, 115431 (2013).
[16] K. Whitham, J. Yang, B. H. Savitzky, L. F. Kourkoutis, F. Wise, and T. Hanrath, Nat. Mater. **15**, 557 (2016).
[17] R. Wang, Y. Shang, P. Kanjanaboos, W. Zhou, Z. Ning, and E. H. Sargent, Energy Environ. Sci. **9**, 1130 (2016).
[18] J. Jang, W. Liu, J. S. Son, and D. V. Talapin, Nano Lett. **14**, 653 (2014).

[19] J.-S. Lee, M. V. Kovalenko, J. Huang, D. S. Chung, and D. V. Talapin, Nat. Nanotech. **6**, 348 (2011).
[20] C.-H. M. Chuang, P. R. Brown, V. Bulović, and M. G. Bawendi, Nat. Mater. **13**, 796 (2014).
[21] T. Chen, K. V. Reich, N. J. Kramer, H. Fu, U. R. Kortshagen, and B. I. Shklovskii, Nat. Mater. **15**, 299 (2016).
[22] J.-H. Choi, A. T. Fafarman, S. J. Oh, D.-K. Ko, D. K. Kim, B. T. Diroll, S. Muramoto, J. G. Gillen, C. B. Murray, and C. R. Kagan, Nano Lett. **12**, 2631 (2012).
[23] E. Talgorn, Y. Gao, M. Aerts, L. T. Kunneman, J. M. Schins, T. Savenije, M. A. van Huis, H. S. van der Zant, A. J. Houtepen, and L. D. Siebbeles, Nat. Nanotechnol. **6**, 733 (2011).
[24] M. Cargnello, A. C. Johnston-Peck, B. T. Diroll, E. Wong, B. Datta, D. Damodhar, V. V. Doan-Nguyen, A. A. Herzing, C. R. Kagan, and C. B. Murray, Nature (London) **524**, 450 (2015).
[25] B. H. Savitzky, R. Hovden, K. Whitham, J. Yang, F. Wise, T. Hanrath, and L. F. Kourkoutis, Nano Lett. **16**, 5714 (2016).
[26] Y. Liu, J. Tolentino, M. Gibbs, R. Ihly, C. L. Perkins, Y. Liu, N. Crawford, J. C. Hemminger, and M. Law, Nano Lett. **13**, 1578 (2013).
[27] W. H. Evers, J. M. Schins, M. Aerts, A. Kulkarni, P. Capiod, M. Berthe, B. Grandidier, C. Delerue, H. S. J. van der Zant, and C. van Overbeek *et al.*, Nat. Commun. **6**, 8195 (2015).
[28] Y. Zhang, D. Zherebetskyy, N. D. Bronstein, S. Barja, L. Lichtenstein, D. Schuppisser, L.-W. Wang, A. P. Alivisatos, and M. Salmeron, Nano Lett. **15**, 3249 (2015).
[29] A. Dong, X. Ye, J. Chen, and C. B. Murray, Nano Lett. **11**, 1804 (2011).
[30] Y. Wu, S. Li, N. Gogotsi, T. Zhao, B. Fleury, C. R. Kagan, C. B. Murray, and J. B. Baxter, J. Phys. Chem. C **121**, 4146 (2017).
[31] E. V. Shevchenko, D. V. Talapin, N. A. Kotov, S. O'Brien, and C. B. Murray, Nature (London) **439**, 55 (2006).
[32] R. E. Chandler, A. J. Houtepen, J. Nelson, and D. Vanmaekelbergh, Phys. Rev. B **75**, 085325 (2007).
[33] H. Lepage, A. Kaminski-Cachopo, A. Poncet, and G. le Carval, J. Phys. Chem. C **116**, 10873 (2012).
[34] H. Lepage, Modélisation de solides à nanocristaux de silicium, Ph.D. thesis, L'institut National des Sciences Appliquées de Lyon, 2013.
[35] I. Carbone, S. A. Carter, and G. T. Zimanyi, J. Appl. Phys. **114**, 193709 (2013).
[36] J. Lee, O. Choi, and E. Sim, J. Phys. Chem. Lett. **3**, 714 (2012).
[37] M. Scheele, J. H. Engel, V. E. Ferry, D. Hanifi, Y. Liu, and A. P. Alivisatos, ACS Nano **7**, 6774 (2013).
[38] L. Qu, M. Vörös, and G. T. Zimányi, Sci. Rep. **7**, 7071 (2017).
[39] X. Chu, H. Heidari, A. Abelson, D. Unruh, C. Hansen, G. Qian, Caroline an Zimanyi, M. Law, and A. J. Moulé, J. Mater. Chem. A **8**, 18254 (2020).
[40] D. Unruh, A. Camjayi, C. Hansen, J. Bobadilla, M. J. Rozenberg, and G. T. Zimanyi, Nano Lett. **20**, 8569 (2020).
[41] See Supplemental Material at http://link.aps.org/supplemental/10.1103/PhysRevB.103.195303 for additional details of the theoretical and experimental methods.
[42] A. Donev, S. Torquato, and F. H. Stillinger, J. Comp. Phys. **202**, 737 (2005).
[43] J. Jasieniak, M. Califano, and S. E. Watkins, ACS Nano **5**, 5888 (2011).
[44] E. M. Miller, D. M. Kroupa, J. Zhang, A. R. Schulz, Philip an Marshall, A. Kahn, S. Lany, J. M. Luther, M. C. Beard, C. L. Perkins, and J. van de Lagemaat, ACS Nano **10**, 3302 (2016).
[45] I. Kang and F. W. Wise, J. Opt. Soc. Am. B **14**, 1632 (1997).
[46] L.-W. Wang and A. Zunger, Phys. Rev. Lett. **73**, 1039 (1994).
[47] J. M. An, A. Franceschetti, and A. Zunger, Phys. Rev. B **76**, 045401 (2007).
[48] C. Delerue, M. Lannoo, and G. Allan, Phys. Rev. Lett. **84**, 2457 (2000).
[49] M. Lannoo, C. Delerue, and G. Allan, Phys. Rev. Lett. **74**, 3415 (1995).
[50] A. B. Bortz, M. H. Kalos, and J. L. Lebowitz, J. Comput. Phys. **17**, 10 (1975).
[51] Y. Liu, M. Gibbs, C. L. Perkins, J. Tolentino, M. H. Zarghami, J. Bustamante Jr., and M. Law, Nano Lett. **11**, 5349 (2011).
[52] R. M. Ziff and S. Torquato, J. Phys. A. Math. Theor. **50**, 085001 (2017).
[53] M. S. Kang, A. Sahu, D. J. Norris, and C. D. Frisbie, Nano Lett. **11**, 3887 (2011).